UNIVERSITY OF TWENTE.

Thermal Activation of the Vortex Mott Insulator to Metal transition

Master thesis - Interfaces and Correlated Electrons

Author:
Martijn Lankhorst

Graduation committee:
Prof. dr. ir. Hans Hilgenkamp
Dr. Nicola Poccia
Dr. Marc Dhallé
Prof. dr. ir. Alexander Brinkman
Prof. dr. Alexander Golubov

November 27, 2014

Abstract

The magnetoresistance of a square array of superconducting islands placed on a normal metal is investigated. This system undergoes magnetic field and current induced phase transitions at rational values of the normalized magnetic field. Scaling analysis is done at integers $f_c = 1$ and $f_c = 2$. This was done previously in [1], where it is argued that the scaling behaviour is similar to that of an electronic Mott insulator, and it is argued that indeed the vortices induced by the magnetic field play the role of the electrons in an electronic Mott insulator. Here, the scaling exponents found in [1] are reproduced, and furthermore the scaling is done at $f_c = 3/2$, which has the same scaling behaviour as the $f_c = 1/2$ transition. Furthermore, by analysing the temperature dependence at the Vortex Mott transitions, it is concluded that the vortices are thermally activated, ruling out the possibility that this Vortex Mott transition is governed by quantum tunneling. Using this mapping from vortices to charges, vortex systems can be used as a tunable laboratory for realizing and exploring quantum many-body systems and their dynamics.

Contents

1 Introduction

After twenty-eight years one of the major problems of physics of how quantum coherence could survive beyond the temperature limits predicted by the BCS theory is still unsolved. Tremendous effort in materials research has resulted in the discovery of new families of relatively high temperature superconductors such as diborides and pnictides, but still a unifying picture is missing. [2, 3, 4, 5]. However some key feature in the last few years could be finally recognized in the so called normal state of those systems, also described as a strange metal.

There is a mounting experimental evidence that high-temperature superconductors needs to take into account both the presence of two electronic components with different orbital symmetry and a nanoscale phase separation involving also the spatial segregation of the spin density, charge density, orbital and local lattice symmetry [6, 7, 8, 9, 10]. Although many indications of multi-component state of matter were coming out from different independent investigations, the multi-scale nature of the phase separation ranging from nanoscale to micro-scale has been definitely established in all the families of high temperature superconductors through scanning X-ray micro and nano diffraction [6, 7, 8, 9]. How the links between the grains in this multi-scale phase separated state of matter could be optimized to enhance the quantum coherence at high temperature is matter of discussion. A search for the key ingredients for this optimum inhomogeneity is indeed gaining momentum, and a proposal – inspired by experimental evidence - about the relevance of a scale invariant geometry for the promotion of high temperature superconductivity has been made [11, 12, 13]. Unfortunately, an experimental model system for a variety of proposed theorems of high temperature superconductivity is currently missing. Regardless, it is tempting to think that since all classes of materials where high temperature superconductivity emerges are made of granular matter, non-equilibrium phenomena relevant for the self-organization of the observed granular patterns should be also present in those system.

There has been a long-standing interest in finding model systems to explore various kinds of phase transitions and one of the most intensely studied area of research in this field is understanding dynamic or nonequilibrium phase transitions for both classical and quantum systems. In most systems there can be considerable disorder or other effects that can make a clear identification and characterization of such transitions difficult. One example of a model system where these ideas can be explored is cold atoms [14, 15] on optical traps where various parameters can be exactly controlled; however, even in these systems it is often difficult to analyse what is occurring since many of the control knobs used in solid state systems to probe the dynamics are missing such as conduction, resistance, and current. As a model system, inspired by the observation with scanning nano X-ray diffraction of a mesoscopic phase separation in all the families of high temperature superconductors, we have mimicked a mesoscopic superconducting phase separated system, designing a nanodevice [1] with regularly spatially segregated superconducting and metallic islands. In this system, using scaling analysis [16], we are able grab the details of the physics of vortex Mott insulator [17, 18] and its dynamic state that is an exemplary manifestation of quantum many-body physics of strongly correlated systems and are thought to be a key ingredient of high temperature superconductivity. In this thesis, we have made a step further by investigating the temperature dependence of the dynamic phase transition, showing the underling microscopic principle governing the dynamic Mott transition through thermal

activation of the vortices.

This report is structured as follows. First the principles of superconductivity and weak superconductivity will be briefly explained. Then a model will be explained worked out describing the properties of JJAs in the superconducting state. In the next section the fabrication process of a JJA is worked out and measurements are shown. Finally two aspects of these measurements are analysed: a) scaling around fractional frustration factors showing the analogy with a Mott insulator and b) temperature dependence to investigate thermal activation versus tunnelling behaviour.

2 Theory of Josephson Junctions

2.1 Superconductivity

A superconductor is a material that loses its electrical resistance when cooled below a certain critical temperature. This effect was first discovered by Heike Kamerlingh Onnes in 1911 in Mercury, and later in other metals. When a material is in its superconductive state, not only does it have zero electrical resistance, it also behaves as a perfect diamagnet, i.e. it expels all magnetic flux lines from its interior. [19]

Ginzburg and Landau discovered a phenomenological theorem now called Ginzburg-Landau theory. It states that the whole superconducting material can be described by one complex order parameter, which is a function of position. The free energy for the superconducting state is expressed in terms of this order parameter, and this order parameter can be found by minimizing this free energy. The magnitude of this order parameter is a measure for the amount of superconducting charge carriers at that position. In this framework, the superconducting transition is a second order phase transition. The GL theorem was able to prove the fact that magnetic flux enclosed in a ring of superconductor must be quantized in units of one flux quantum, called Φ_0, and prove that $\Phi_0 = h/2e$. Another important result is the proximity effect. The theorem shows that in a superconductor-normal metal interface, the order parameter is not directly zero in the metal, but rather it decays in a small region, explaining the name proximity effect. This length scale is called the coherence length.

In 1957 a theorem was discovered which could explain the microscopic origin of superconductivity. It was discovered that electrons form pairs, called Cooper pairs, and it are these Cooper pairs which can move trough the superconductor without resistance. The pairing occurs by a phonon-mediated attractive force. This state is a bosonic state, so all cooper pairs collapse into the same state, which explains why the state can be described with one order parameter.

In 1986 Bednorz and Müller discovered that a class of ceramic materials called cuprates are, contrast to what BSC theorem predicts, superconducting, and the critical temperature was much higher than BSC theorem could explain. These materials are called High Temperature Superconductors, or HTS. These materials are layered materials with Copper-Oxide planes, and the superconductivity occurs in these planes. Although phenomenologically HTS are well understood, the microscopic origin of this effect is still unknown and remains one of the biggest unsolved problems in physics today.

2.2 Weak Superconductivity

Weak Superconductivity is the effect that a superconducting current can occur in a tunnel junction of two superconductors. The maximal current that can tunnel without resistance is generally much smaller than the critical current of the leads, explaining the term. This effect is called the first Josephson effect, or DC Josephson effect. In addition, a when larger current is sourced, the junctions starts emitting high-frequency electromagnetic waves. This is called the AC Josephson effect. In most of this report, SNS (S standing for superconductor, N for normal metal) tunnel junctions will be considered, although there are many different kinds.

Weak superconductivity is possible due to the proximity effect. Intuitively, due to the weak link the whole material condenses into one superconducting wave function, with the

property that the magnitude must be Ψ_0 in both superconductors, but the phase can differ. Inside the weak link the magnitude of the wavefunction is suppressed, and the exact functional form is such that the free Ginzburg Landau energy is minimized. An important quantity is this phase difference, which obeys the following relation:

$$I_s = I_c \sin\theta \tag{1}$$

Where $\theta \equiv \phi_2 - \phi_1$ is the phase difference from a point well inside the second superconductor to a point well inside the first superconductor. This is called the first Josephson equation, and is a universal relation for any weak link, the value of I_c depends on the geometry and type of the weak link, and the materials involved. This value is the maximum current that can be sourced through a weak link without resistance.

If one sources a current larger than I_c, an RF-EM field is generated. This is called the AC Josephson effect, and is a direct consequence of the second Josephson equation:

$$2eV = \hbar \frac{\partial \theta(t)}{\partial t} \tag{2}$$

It relates the voltage across the weak link to the time derivative of the phase difference across the weak link. This can be derived by interpreting the superconducting wavefunction as an eigenfunction of a Hamiltonian with some energy level E and plugging it into the Schröödinger equation. One assumes explicitly that only the phase difference can be a function of time.

2.3 RSCJ model

The Resitivly Shunted model of a Josephson junction (RSJ) explains why RF radiation occurs. It states that when a current larger than the critical current of the JJ is sourced, the supercurrent is described by equation 1, but in addition, there is a normal ohmic current path in parallel. The resistance of this path is called the normal state resistance R_n and depends on many parameters like I_c. If one works out this model for a constant current, one finds that the voltage is oscillating with frequency ω and mean voltage $\bar{V}$:

$$\omega = \frac{2eR_n}{\hbar}\sqrt{I^2 - I_c^2} \tag{3}$$

$$2e\bar{V} = \hbar\omega \tag{4}$$

Equation 4 suggest that the RF radiation consist of photons that are generated by the electrical energy that the cooper pairs loose when they tunnel through the junction. In general one can also add a parallel capacitor to the model. The equation of motion for the complete RSCJ system is:

$$I = I_c \sin\theta + V/R + C\frac{\mathrm{d}V}{\mathrm{d}t} \tag{5}$$

or

$$\frac{\mathrm{d}^2\theta}{\mathrm{d}\tau^2} + Q^{-1}\frac{\mathrm{d}\theta}{\mathrm{d}\tau} + \sin\theta = I/I_c \tag{6}$$

Where $\tau = \omega_p t$ and $\omega_p = \sqrt{2eI_c/\hbar C}$ is the plasma frequency of the junction, and $Q = \omega_p RC$ is called the quality factor.

2.4 Tilted washboard potential

The problem of weak superconductivity can be formulated differently with the tilted washboard model. This will give further physical insight, and it considers the potential energy as a starting point.

Maintaining a supercurrent costs no energy, but setting up a supercurrent in a JJ does cost energy; the kinetic energy of the electrons and Josephson energy. The second can be derived as follows. When one ramps the current I_1 at $t = t_1$ to I_2 at $t = t_2$, a potential difference arises across the junction because the phase is ramped from θ_1 to θ_2. The resulting necessary power must be integrated over time to obtain the Josephson Energy:

$$E_j = \int_{t_0}^{t_1} U(t)I(t)\mathrm{d}t = \int_{t_0}^{t_1} \frac{\hbar I_c}{2e}\sin\theta(t)\frac{\partial\theta(t)}{\partial t}\mathrm{d}t = \frac{\hbar I_c}{2e}(\cos\theta_1 - \cos\theta_2) \tag{7}$$

Note, this is the energy contained in the supercurrent. In addition to this energy, there is also a dissipative energy term due to the current going through the resistor, and there is energy stored in the capacitor.

One can arrive at the potential energy formulation as follows. First one multiplies equation 6 with $\hbar I_c\dot{\theta}/2e$:

$$(\frac{\hbar I_c}{2e}\sin\theta + \frac{\hbar I}{2e} + \frac{\hbar I_c}{2e}\ddot{\theta})\dot{\theta} = -\frac{\hbar I_c}{2eQ}\dot{\theta}^2 \tag{8}$$

One can identify this as $\frac{\mathrm{d}E}{\mathrm{d}\tau} = -\dot{q}$ where E is the total energy of the system and $\dot{q}$ is the heat flow out of the system. Then:

$$E = \frac{\hbar I_c}{2e}(1 - \cos\theta) - \frac{\hbar I}{2e}\theta + \frac{1}{2}\frac{\hbar I_c}{2e}\dot{\theta}^2 \tag{9}$$

$$\dot{q} = \frac{\hbar I_c}{2eQ}\dot{\theta}^2 \tag{10}$$

Then, in analogy to classical physics, one can identify E as $E_{\mathrm{kin}} + U$, where:

$$U = \frac{\hbar I_c}{2e}(1 - \cos\theta) - \frac{\hbar I}{2e}\theta \tag{11}$$

This potential looks like a tilted washboard. Because the equations are the same as in classical mechanics, the standard interpretation for potential energy carries over, so a system is in equilibrium if the potential is at a local minimum, and if enough extra kinetic energy is added to the system it will overcome potential barriers etc. Note that the kinetic energy in this interpretation is actually the energy stored in the capacitor $\frac{1}{2}CV^2$. Also note, in equilibrium there is no heat dissipation.

The potential is sketched in figure 1. As $I > I_c$, the local minimum disappears and the superconducting state also disappears. The local minimum θ_m corresponding to the equilibrium state obeys the relation $I = I_c\sin\theta_m$, as it should.

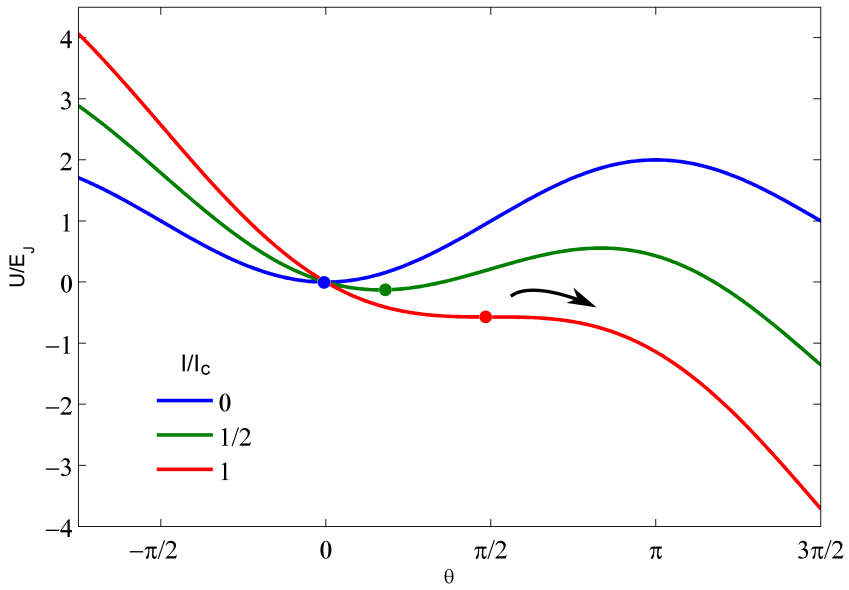

Figure 1: Tilted washboard potential drawn for various currents. A local minimum in the potential (the dots in the figure) corresponds to the equilibrium state. As the current is increased to the critical current, the minimum disappears and the phase starts to slip.

In the case $Q << 1$, which corresponds to the RSJ model, one can see in this picture that the dissipation heat term becomes very large. This means that motion in the classical analog is damped, so junctions with this property are called overdamped junctions. The opposite case of $Q >> 1$ corresponds to underdamped junctions. In the case of underdamped junctions, hysteresis in the IV curves can occur, or in other words the current needed to expel the system from a potential well when sweeping the current up is not the same as the current needed to retrap the system in a potential well during the downsweep. The expelling happens at I_c, the retrapping happens at a current $I_r < I_c$ because the system needs to be slowed down by heat dissipation to be trapped back, which is very small in the underdamped case.

2.5 Finite temperature effects

For the discussion above it is assumed that $T = 0$, in this section will be explained what conceptually happens to Josephson Junctions at finite temperatures. This will be explained in the tilted washerboard model, where temperature induces an extra energy $k_B T$ to the system. This extra energy can cause the system to excite over the potential barrier with some finite probability proportional to the factor $\exp -\frac{\Delta U}{k_B T}$. As long as the system stays in the potential well, the thermal energy causes the system to oscillate in the well with the plasma frequency $\omega_p/2\pi$, which can be roughly interpreted as the frequency of attempts to excite over the barrier. Besides this thermal activation over the potential barrier, it is also

possible to have quantum tunnelling through the potential barriers in small junctions, as discussed in section 6.

The thermal activation has different consequences in the two limits of overdamped and underdamped junctions. In overdamped junctions, when the system is thermally excited over the potential barrier, it gets immediately retrapped in the next potential well, from which the process repeats. Ambegaokar and Halperin theory[20] describes the resulting IV curves as a function of temperature, which can be used to fit experimental IV curves to obtain the ratio of I_c/T, which will be used later in the report. In the underdamped case, if the system is excited over the potential barrier, it will not immediately retrap but gets accelerated up to a terminal velocity which corresponds to some voltage V_t. This means that there is in fact a distribution in current at which the system loses its conductivity, but the mean of that distribution will be smaller than I_c at $T = 0$.

3 Josephson Junction Array

In this section it will be discussed how one can generalize the concept of weak superconductivity to systems with multiple Josephson junctions. These systems are called Josephson Junction Arrays or JJAs. As for single Josephson Junctions, it can be described both with the RSCJ model and with the tilted washboard model.

A JJA can be mathematically described with a graph, with as vertices the superconducting islands, and as edges the Josephson Junctions coupling the islands. The following notation is used throughout this section. The entire graph, g, contains all edges E and all vertices V (denoted $g(E, V)$). An edge from vertex i to vertex j is called edge (ij). A cycle p is a subgraph with a subset of edges and a subset of vertices, such that the edges form a cycle. The set of all cycles in g is called P. The set of all edges in an array is sometimes referred to in a vector, for example $\vec{\theta}$ means $(\theta_{12}, \theta_{13}, \theta_{23}, ...)$, where by convention the order of edges is ascending. Similarly the set of all vertices is sometimes also used in a vector.

3.1 Flux Quantization in JJAs

In this section the concept of flux quantization in JJAs is discussed. For each cycle $p \in P$, one can take a closed path integral in real space, along the islands corresponding to the vertices in the cycle, over the second Ginzburg-Landau equation. It is assumed that the path is taken well inside the superconductor such that $v_s = 0$ along the whole loop [19].

$$\forall p \in P : \oint \nabla\phi \cdot \mathrm{d}\vec{l} = \frac{2\pi}{\Phi_0} \oint \vec{A} \cdot \mathrm{d}\vec{l} \text{ along a loop corresponding to cycle } p \tag{12}$$

Where the right side is equivalent to the magnetic flux through the loop. Because the superconducting phase is constant on the superconducting islands and only changes in the weak links, the left hand side can be rewritten to a sum of phase differences, θ_{ij}. So θ_{ij} is the phase difference between islands i and j, and $\theta_{ij} = -\theta_{ji}$. This is sketched for one cycle in a JJA in figure 2. Note that because ϕ is multi valued, so is θ, but with no loss of generality one can assume that $\forall (ij) \in E, \vec{\theta}_{ij} \in [-\pi, \pi)$, because if one adds 2π to a phase, all physically measurable quantities are not changed.

One can rewrite equation 12. Some graph theory notation is used. $E(g)$ means the set of all edges in graph g, one particular edge is represented by (ij) meaning the edge going from vertex i to vertex j.

$$\forall p \in P : \sum_{(ij) \in E(p)} \theta_{ij} = 2\pi(f_p - n_p) \tag{13}$$

Where $f_p = \frac{\Phi_p}{\Phi_0}$ and Φ_p is the magnetic flux going through a loop corresponding to cycle p. Furthermore, n_p must be integer values. The system of equations 13 is a linear system in the variables θ_{ij}. The equations corresponding to different loops can be linearly dependent, so only a subset of the loops is needed to obtain all flux quantization rules. In appendix A will be proven that for a square lattice it suffices to take the loops around all the elementary squares, so to each square an integer number of flux quanta is attributed.

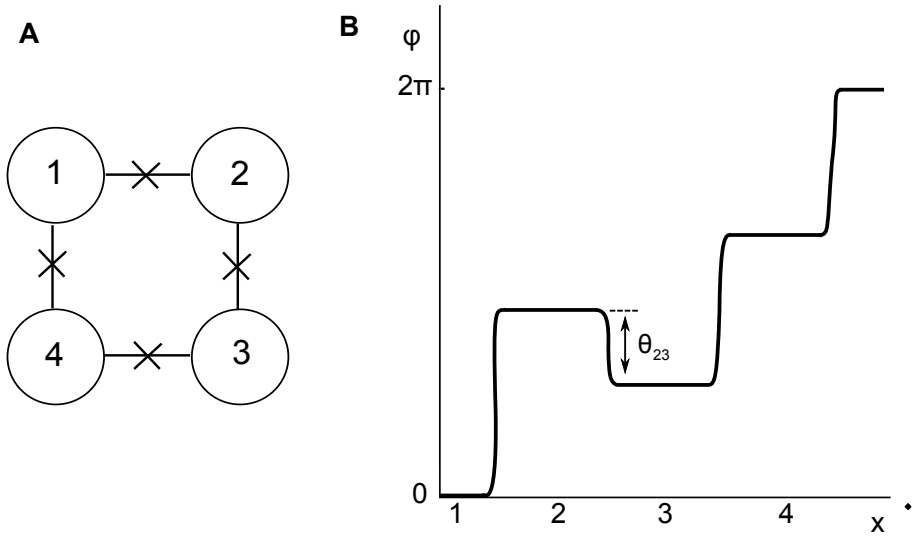

Figure 2: **Flux Quantization** (**A**) part of a JJA containing 4 islands and 4 junctions. (**B**) Sketch of the superconducting phase along the loop corresponding to the cycle (1 2 3 4 1). The x-axis represents the distance coordinate along the loop and the numbers correspond to the islands (in this case, $f - n = 1$, see eq. 13).

3.2 RSCJ model for JJAs

The RSCJ model can be generalized to arbitrary arrays by first setting up Kirchhoff's rules and then substituting the currents corresponding to each junction with the RSCJ current for that junction. The Kirchhoff rules can be written as $M\vec{I} = \vec{I}_{\text{ext}}$, so:

$$M(I_c \sin\vec{\theta}(t) + \frac{\hbar}{2eR_n}\frac{\partial\vec{\theta}(t)}{\partial t} + C\frac{\hbar}{2e}\frac{\partial^2\vec{\theta}(t)}{\partial t^2}) = \vec{I}_{\text{ext}} \tag{14}$$

Here it is assumed that the critical current I_c and the normal state resistance R_n are the same for each junction, but one can relax this assumption. Combining these equations with the flux quantization rules completely describes the superconducting phase evolution of a JJA at zero temperature. These two sets of equations together will be called the RSCJ system. A special case is if all currents are smaller than their respective critical current, then one obtains the equilibrium state:

$$MI_c \sin\vec{\theta} = \vec{I}_{\text{ext}} \tag{15}$$

3.3 Tilted Washboard Potential for JJAs

One can also generalize the tilted washboard model to arbitrary arrays. Here only the result is stated, it is proved in appendix A. The equilibrium states of the RSCJ sytem can be

found by finding the critical points of a tilted washboard potential U, where the direction of the tilt is now dependent nontrivially on the islands where the external current is injected and the structure of the underlying graph of the array. Without an external current this system reduces to the Frustrated XY Model [21]. I have not been able to find any reference which also describes the full tilted washboard model. Note, from the general interpretation of the tilted washboard potential for one junction, it is clear that saddle points are not actual physical equilibria, and it is assumed that only the local minima in U are physical solutions.

Given an external magnetic field B, an external current $\vec{I}_{\text{ext}}$ smaller than the critical current and a vortex configuration $\vec{n}$, the phases of the equilibrium state of a JJA described by the graph $g(E, V, P)$ at zero temperature can be found by finding local minima to:

$$U = \sum_{(ij)\in E} (E_{c;ij}(1 - \cos\theta_{ij}) - c_{ij}\theta_{ij} I \Phi_0) \tag{16}$$

subject to:

$$\forall p \in P : \sum_{(ij)\in E(p)} \theta_{ij} = 2\pi(f_p - n_p) \tag{17}$$

$$\forall (ij) \in E, \theta_{ij} \in [-\pi, \pi) \tag{18}$$

where $\vec{c}$ must satisfy:

$$M\vec{c}I = \vec{I}_{\text{ext}} \tag{19}$$

Here M is the matrix representing the Kirchhoff's equations. It is yet an open question if in this formulation there is a unique solution $\vec{\theta}$ for all the input. The maximal current is defined as the largest value of I for which a minimum exists in U.

3.4 Vortices and band structure

In the model, the number n_p can be interpreted as the number of vortices on plaque p. If one calculates the current configuration around vortices, one obtains a circulating current around all the vortices, and the magnitude of these currents is approximately $I = I_c \sin\frac{\pi}{2}(f_p - n_p)$. In section 3.6 one can see examples of this. In an experiment, one does not control the vortex numbers $\vec{n}$. One applies an external field and an external current, and the system finds an equilibrium state in which the energy, defined as follows, is minimal:

$$E = \sum_{(ij)\in E} E_{J;ij}(1 - \cos\theta_{ij}) \tag{20}$$

This energy can calculated as a function of current, field and vortices, one gets a band structure $E_{\vec{n}}(B, I)$, where discrete bands form because the vortex numbers are quantized. The ground state is then the vortex configuration with the lowest energy. For a particular vortex configuration $\vec{n}$, there does not have to be a solution for all values of B and I, this happens if there is no local minimum to the potential.

An important property is that the spectrum is periodic in B. In the case where all elementary plaques have the same area, one can see that if one adds the value 1 to f, one can add the value 1 to all components of $\vec{n}$, and the equations will be unchanged, so the solution will be also. In the general case, the condition is: find the smallest magnetic

field B_p such that $\forall p \in P, f_p \in \mathbb{Z}$. Then a state is periodic in this magnetic field B_p, i.e. $E(B + B_p) = E(B)$. Interestingly, this means that if one finds a ratio between two plaque areas which is non-rational, then a state is not periodic in the magnetic field. In more detail; given the vector of all plaque areas $\vec{A} = (A_1, A_2, ..., A_N)$, and one defines $f \equiv \frac{B}{B_p}$ and $f_i \equiv \frac{BA_i}{\Phi_0}$, then one finds:

$$B_p = \frac{\Phi_0}{\gcd\,(\frac{\vec{A}}{A_i})A_i} \text{ (where any i works)} \tag{21}$$

$$f = \gcd\,(\frac{\vec{A}}{A_i})f_i \tag{22}$$

There are some hypothesis specific to square arrays that are to my knowledge not yet proven but important to note:

1. The ground state energy as a function of magnetic field is thought to be the ground state energy of the Hofstadter butterfly [22, 23]

2. The critical current as function of magnetic field forms a local maximum around rational values of f.

3. At a rational value of f, $f = p/q$, it is believed [24] that in an infinite square array the ground state vortex configuration is spatially periodic with period q, so the vortex configuration is the same on squares of q by q elementary plaques.

This suggests a deep connection between the Hofstadter problem of the spectrum of 2D electrons in a periodic potential subject to a perpendicular external magnetic field. However, for an atomic potential, the period is of the order of angstroms and the fields necessary to probe this effect is on the order of 10^5T, but with vortices one can control the distance between the islands and thus the period of the potential. This reduces the periodic field B_p to the order of mT for inter island distances of the order of μm.

3.5 Vortex interactions

In the ground state of a square JJA with no external magnetic field and currents, all phase differences are zero and there are no vortices. One can create an excited state by putting a single vortex in the array. The energy of this state can be approximated by [19]:

$$E = \pi E_J \ln \frac{R}{a} \tag{23}$$

where R is the radius of the array and a the length of the side an elementary plaquette. This is the energy which is required to induce either a vortex or an antivortex. Now, if one places both a vortex and an antivortex, the energy needed to do this is:

$$E_{12} = 2\pi E_J \ln \frac{R_{12}}{a} \tag{24}$$

where now R_{12} is the distance between the vortices. This implies there is an attractive force between two vortices of opposing sign. Similarly, there is a repelling force between

vortices of the same sign. An analogy can be made between vortices in a JJA and charged particles in a coulomb gas, called a charge-vortex duality. The mapping $\pi E_J \rightarrow Q^2$ maps the vortices to charges such that the force law is the same. In addition, not only do the vortices experience a coulomb like force, they also experience a force that pins them to the lattice. An analogy can be made between the physics of electrons in a Mott insulator and that of vortices in a JJA. In section 5 it is shown that these vortices undergo a phase transition which can be shown to have similar scaling behaviour to that of an electronic Mott transition.

3.6 Computer experiments on Finite Josephson Junction Arrays

As a proof of concept, a zero field vortex excitation and a vortex-antivortex excitation are calculated with the Tilted Washboard Potential for Arrays model. This is done in a square lattice of 10 by 10 islands with grounding bars on both sides. In all images, the number assigned to the edges is the current, where $I_c = 1$ for all junctions is assumed. In figure 3 a single vortex is placed in the centre, no external field is applied and an external current is sourced through the bars. Note that a current of I_c circulates around the plaque where the vortex is placed, showing that the abstract definition of vortices in the model actually corresponds to physical vortices. In figure 4 a vortex-antivortex pair excitation is shown. Some different vortex-antivortex configurations have been tested and qualitatively the relation that the energy increases as the core-to-core distance increases is confirmed, showing that also in this model vortices attract antivortices.

For this system some states of the energy spectrum are obtained, see figure 5. For this the total energy is calculated for different vortex configurations as a function of magnetic field. The vortex configurations used are the ground states at $f = 0, f = 1/3, f = 1/2, f = 2/3$ and $f = 1$, see figure 10. This is merely the framework of the spectrum, in principle one must do this for *any* vortex configuration, not just the 5 chosen configurations. In appendix D the ground state configurations of $f = 1/2$ and $f = 1/3$ are shown.

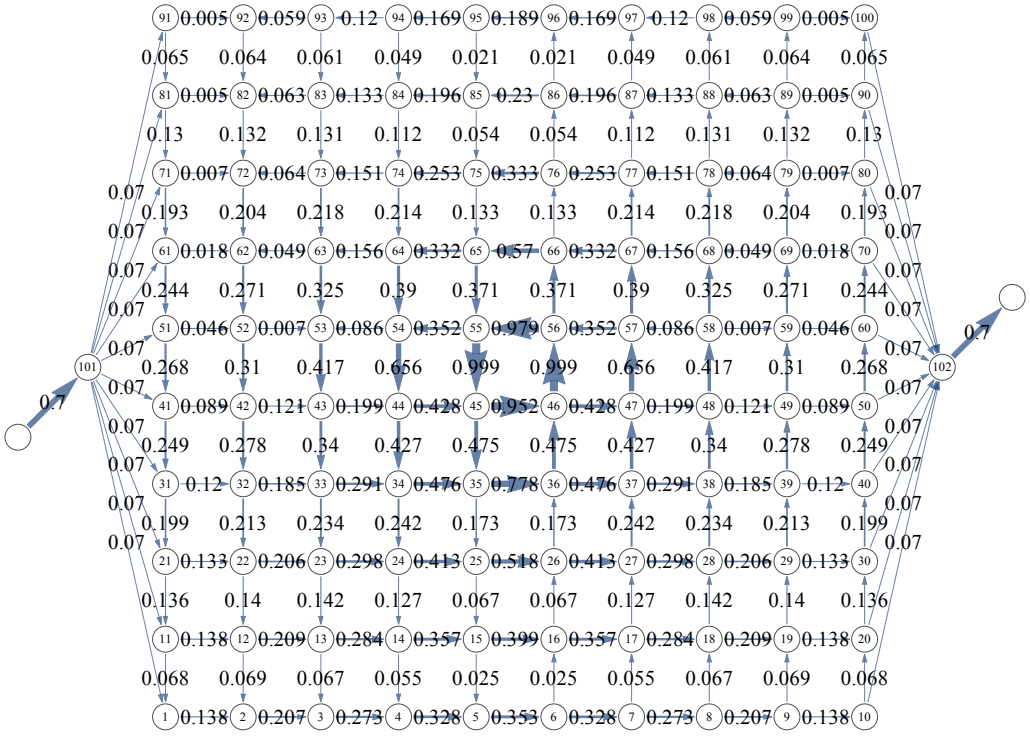

Figure 3: Current distribution in an array with one vortex in the centre square with an external current of 0.7 and no external magnetic field. All critical currents are assumed to be 1. The energy of this state $E = 9.6E_J$.

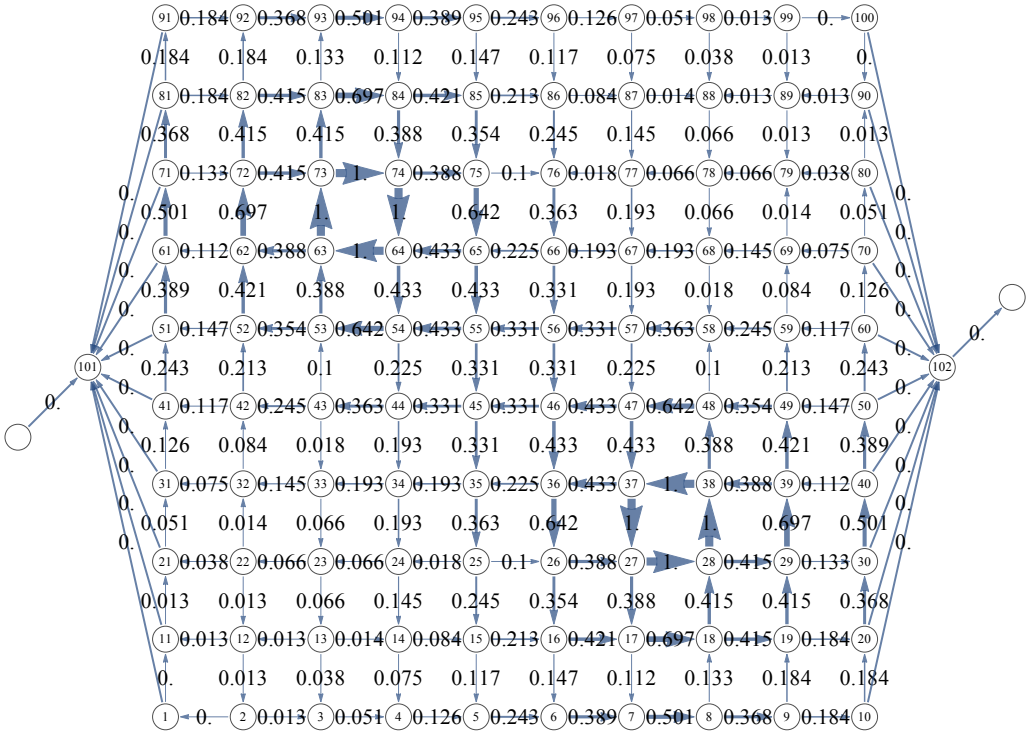

Figure 4: Current distribution in an array with a vortex-antivortex pair with no external current and magnetic field. All critical currents are assumed to be 1. The energy of this state $E = 15.6E_J$.

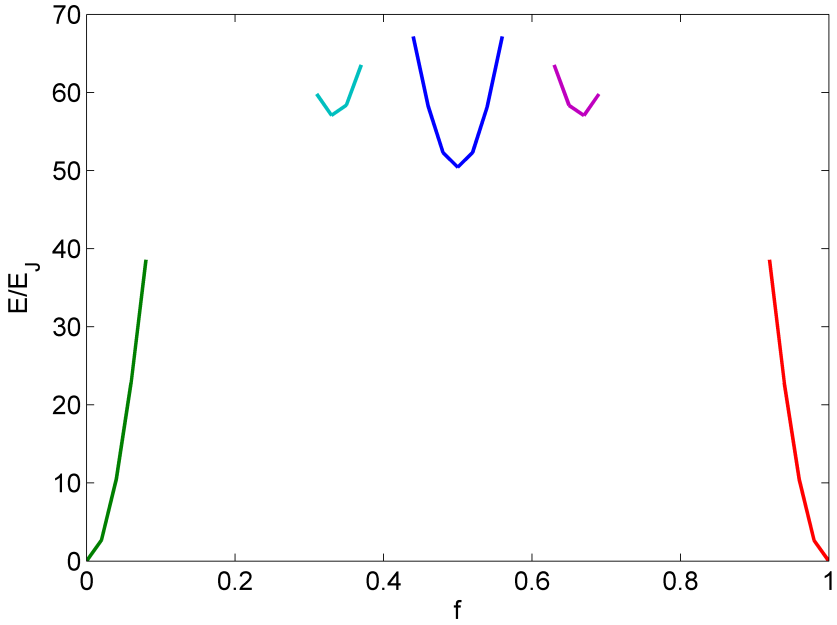

Figure 5: Incomplete energy spectrum of the array calculated for different vortex configurations as a function of magnetic field. The vortex configurations used are the ground states at $f = 0, f = 1/3, f = 1/2, f = 2/3$ and $f = 1$.

4 Experimental realization Josephson Junction Array

4.1 Sample fabrication and experimental setup

Josephson junction arrays of niobium islands on top of a thin layer of gold were fabricated. In figure 6 a schematic top view and side view of the sample is given. The samples are grown on Si/SiO_2 substrates. A 40 nanometer thick gold layer is grown with photo lithography and sputter deposition. The gold layer consists of a central square of 80 by 80 micron with in each corner a terminal which can be wirebonded to the electronics. On top of the central gold square, an array of 300 by 300 Nb islands are grown with e-beam lithography and sputter deposition. The islands are approximately 45nm high, the distance from centre to centre $a = 250$nm, and the diameter is 168nm. In figure 7A a SEM image of the Nb islands is shown. On the side of the sample two Nb bars are patterned to ensure the current goes through the array of islands homogeneously. All measurements shown in the rest of this report are done on a single sample. Variations of island spacing and thickness were systematically done by S.Eley et al. [25], on triangular lattices but not as a function of magnetic field.

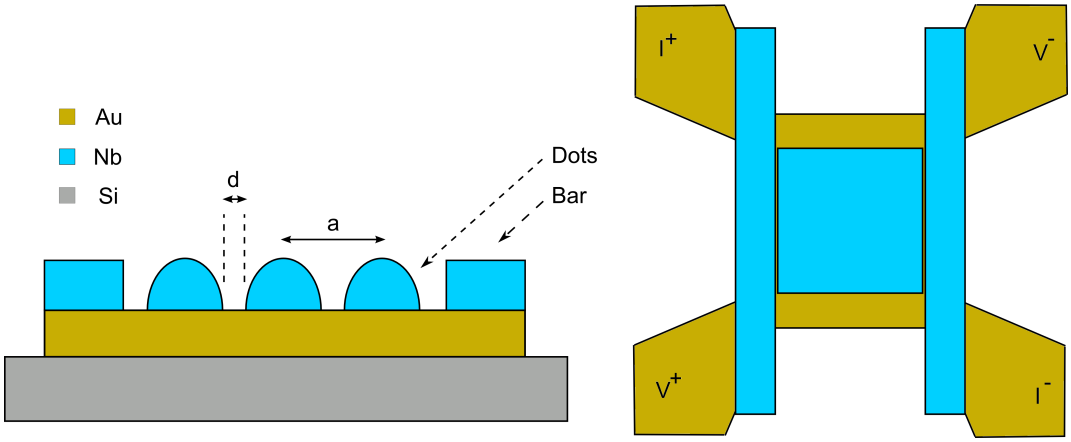

Figure 6: Schematic side view and top view of the sample.

The IV curves are measured in a 4-point configuration at a temperature below the critical temperature of niobium, which is 9.2K. Below this temperature the Nb bars become equipotential, so in effect the potential difference between the two Niobium bars is measured as a function of the current going through it. In appendix B the circuit diagram is shown. In addition an external field is applied whose field lines are perpendicular to the plane of the sample. Measurements are done in a bath cryostat in liquid helium, where the boiling temperature of helium is controlled with an external mechanic pump and a valve. A DT400 temperature sensor is mounted in the fluid at the same height of the sample. With this setup temperature can be controlled between approximately 1.5K and 4.2K, although systematic errors can occur because 1) the temperature sensor is only calibrated above 2K and 2) no heater could be used in this setup.

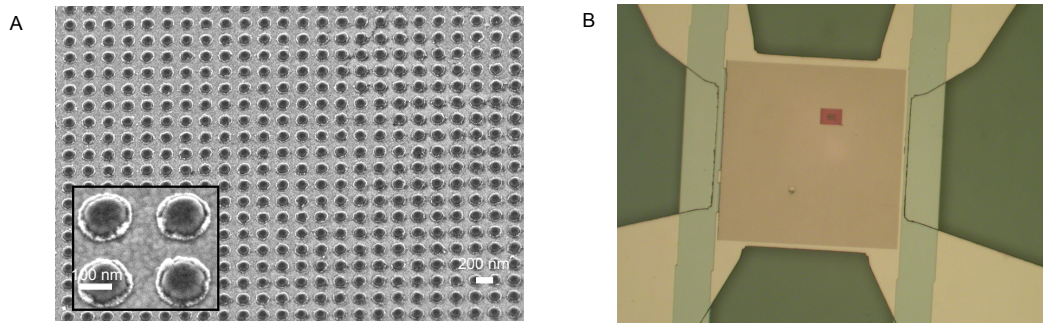

Figure 7: **Device images** (**A**) SEM image of the fabricated Josephson Junction arrays showing the Niobium islands on top of gold (**B**) microscope image of the whole sample including the Nb bars and the contact pads.

4.2 Sample characterization

When the Niobium is cooled below the critical temperature, the niobium becomes superconducting and the niobium islands become proximity coupled trough the gold, forming SNS junctions. The coherence length of Niobium is approximately 35nm at zero temperature [26] and remains constant up to very near the T_c where it diverges. The ratio $d/\xi \approx 2.3$ determines the critical current for the junctions, $I_c \propto \exp -d/\xi$.

First, the voltage was measured as a function of current and magnetic field at $T = 4.2$K. In figure 8A the resistance V/I is plotted as a function of magnetic field and current. In the rest of this section some interesting features are shown and analysed.

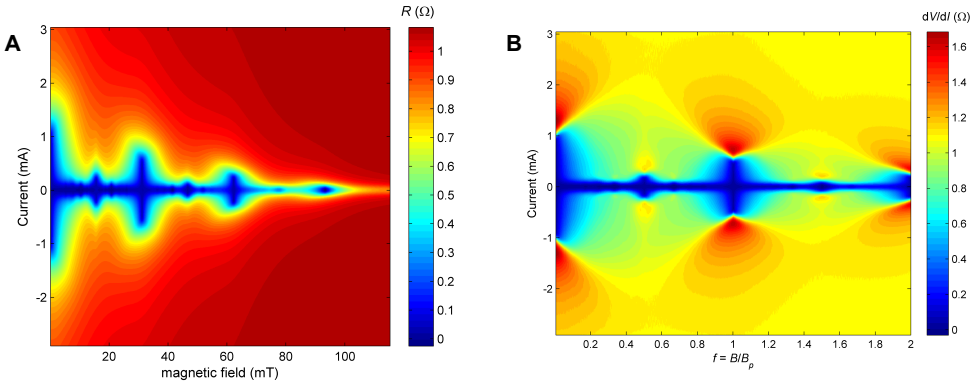

Figure 8: Measured resistance (**A**) and differential resistance (**B**) as a function of magnetic field and current at 4.2K.

At a fixed field, an IV curve looks qualitatively like that for an overdamped Josephson

junction (see figure 11), and the IV curves are non-hysteretic. The critical current is a complicated function of magnetic field. A measure for the critical current is determined with a voltage threshold of 50μV and of 2μV, see figure 9. For a square array of Josephson junctions, one expects the critical current to be periodic in the magnetic field with a period $B_p = \Phi_0/A$ where A is the area of one elementary square. This value is $33.0m$T, which corresponds approximately with the measured value of $31.1m$T. The difference is attributed to an error in the calibration of the magnetic field. One can see that the periodicity does not completely hold because the critical current is damped. This could possibly be attributed to the broadness of the junctions, causing destructive interference between loops around an elementary plaque which can have slightly different enclosing areas. The same happens in extended junctions [19].

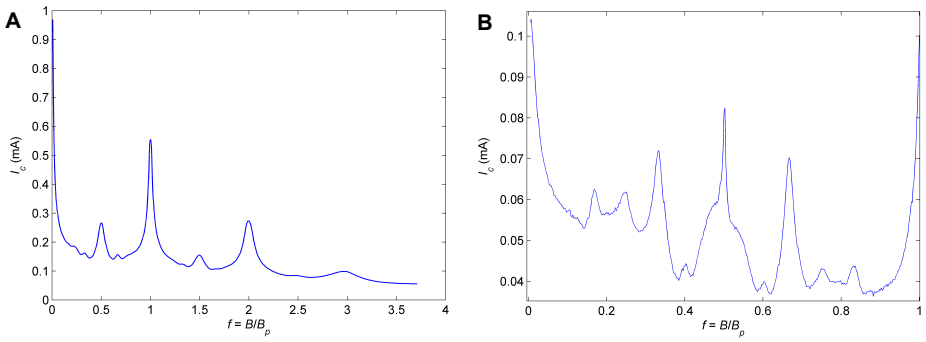

Figure 9: **Critical current** (**A**) Critical current as function of magnetic field determined by a voltage threshold of 50μV. (**B**) Critical current as function of magnetic field determined by a voltage threshold of 2μV. Peaks can be seen at fractions $f = 1/6, 1/4, 1/3, 2/5, 1/2, 3/5, 2/3, 3/4, 5/6$.

A second striking feature is the peaks in critical current at rational values of $f = B/B_p$. This is explained by ordering of the vortex configuration at these values. The number of vortices present in the array in the ground state is approximately f times the number of elementary plaques. Then at rational values $f = p/q$, it is proposed that the vortices form a q by q unit cell which is repeated. For some values of f these patterns are shown in figure 10. One can argue that these states are ground states because they minimize the potential energy, or alternatively argue that these configurations allow the vortices to be as far as possible away from each other because the vortices mutually repel each other. These ordered states can support a higher supercurrent before entering the dynamic state, or in the tilted potential picture have deeper potential wells. Especially in figure 9B a much smaller voltage threshold is used and many fractions become visible, notably $1/6, 1/4, 1/3, 2/5, 1/2, 3/5, 2/3, 3/4, 5/6$.

It is not shown in this data, but if one sweeps back from high to low field, the graph looks the same. From this it can be concluded that if one sets a field to a specific value of f, the vortices quickly rearrange themselves in a energetically favourable configuration with exactly $90000f$ vortices. However, at very low temperature it might be possible that hysteretic effects can occur, especially around rational frustration factors.

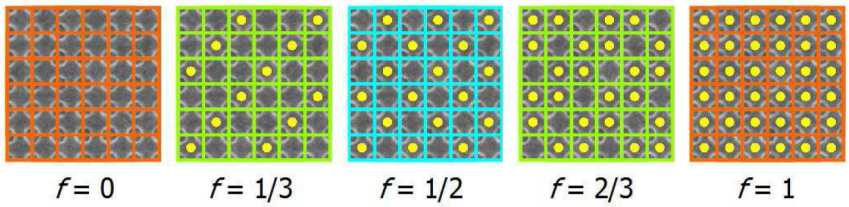

Figure 10: Ground state vortex configurations at various values for f. The yellow dots correspond to vortices which sit in the middle of a plaque of four islands. [1]

In this section the shape of the IV curves will be analysed. In figure 11 Ambegaokar Halperin theory is used to fit the IV curve at $B = 0\text{T}$, $T = 4.2\text{K}$. The fitting is done in three parameters, I_c, the barrier strength $u = \Delta U/k_BT$ and an offset resistance R_{off}, which is the slope of the IV curve at $T = 0\text{K}$. From this the values $I_c = 1.33m\text{A}$, $u = 20.5$, $R_{\text{off}} = 20m\Omega$ come out. The finite offset resistance is attributed to a distance between the Nb bars and the islands being larger than d. The fit works well in the limit of high current, but at small currents there seem to be two critical currents in the measured data. If one sets up a small magnetic field $B << B_p$ as shown in figure 12, the transition at the first critical current seems to become more visible. If one does this around $f = 1$, one can also see these two critical currents, while around $f = 1/2$, there is only one critical current visible. This observation has been done before on antidot arrays [27], where the intermediate state was attributed to partial disorder of the vortex lattice and was called plastic vortex flow. Note that the two different voltage thresholds used to obtain I_c in figure 9 approximately probe the crossover currents of these two different transitions.

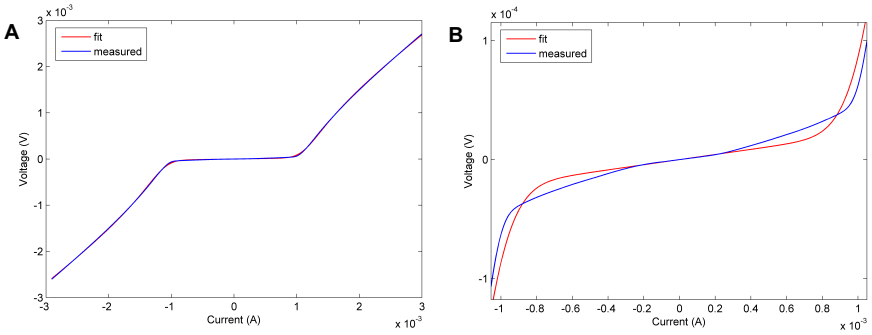

Figure 11: **Ambegaokar Halperin fit at** $f = 0$ (**A**) Fit of the zero field IV curve using Ambegaokar Halperin theory. The parameters found are $I_c = 1.33m\text{A}$, $u = 20.5$, $R_{\text{off}} = 20m\Omega$, $R_n = 0.98\Omega$. (**B**) Same fit as panel (**A**) but zoomed in. One can see there are two transitions which the AH theory cannot explain.

Another important feature is that the differential resistance $\text{d}V/\text{d}I$ as a function of I shows inversions around rational values of f, whereas these inversions are not present in

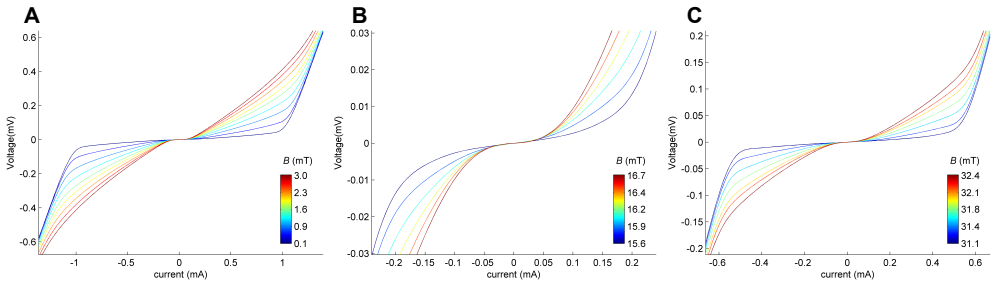

Figure 12: $V(I)$ **curves around critical frustration factors** (**A**) IV curves at magnetic field values close to $f = 0$. The two transitions are clear. (**B**) IV curves at magnetic field values close to $f = 1/2$. The shape of the curves is qualitatively different than those at $f = 0$ and there seems to be only one transition (the second transition seems to be there but very hard to see). (**C**) IV curves at magnetic field values close to $f = 1$. The shape of the curves is qualitatively the same as those at $f = 0$ with two transitions.

the resistance curves, as discussed in [1]. The differential resistance is shown in figure 8B. This inversion can be seen more clear if one plots the differential resistance as a function of magnetic fields at various currents, as shown in figure 13B. In section 5 these inversions are analysed more closely, where it is argued that this is in fact a vortex Mott insulator to metal transition, and it obeys a scaling law. Reference [27] also did experiments where this inversion is visible.

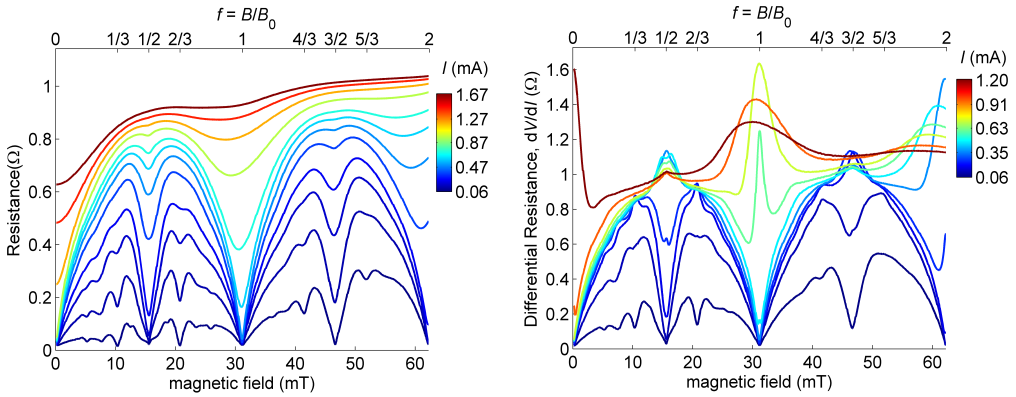

Figure 13: Measured resistance (**A**) and differential resistance (**B**) as a function of magnetic field and current at 4.2K. The curves are periodic in the magnetic field, B_p, with a period of $31.1mT$ which corresponds to the field at which one flux quantum of external field is trapped in one elementary plaque. Also at rational values of f the resistance shows dips, while the differential resistance shows a transition from dips into peaks as current is increased.

5 Scaling analysis and the Mott transition

In this section scaling behaviour in the (I, B) phase space is investigated, closely following [1]. Around critical points (I_c, f_c) the scaling behaviour of $|I - I_c| \propto |f - f_c|^{(\delta-1)/\delta}$ is found, where $\delta = 3$ for integer f_c and $\delta = 2$ for values of f_c with denominator 2. The scaling for $f = 1$, $f = 2$ and $f = 1/2$ is also done in [1] where the same exponents are found. The scaling at $f = 3/2$ is new.

5.1 Vortex Mott Insulator to Metal transition

This scaling is attributed to the many body physics of the sea of vortices, which behaves similarly to the sea of electrons in a Mott Insulator [1]. In a Mott insulator, ordinary band structure would predict the material to be a metal, but the strong coulomb repulsion can localize the electrons to the lattice sites. So, in $U - T$ phase space it undergoes a Mott Insulator to metal transition. In the case of vortices, the magnetic field sets the vortex density, and vortices repel, analogous the Coulomb force for electrons. So B plays the role of U, and sea of vortices undergoes a phase transition from a pinned Mott-Insulating state below the critical current to a metallic state above the critical current. Qualitatively, the current in a vortex Mott insulator plays the same role as temperature in a electronic Mott insulator, for both drive the Mott insulator to a metal upon increasing. So the mapping $|U - U_c| \to |f - f_c|$ and $|T - T_c| \to |I - I_c|$ is proposed, with critical point $(U_c, T_c) \to (f_c, I_c)$. Around this critical points it is investigated whether the scaling behaviour $|U - U_c| \propto |T - T_c|^{(\delta-1)/\delta}$ [28, 29] in an electronic Mott Insulator can be mapped to the scaling behaviour for a Vortex-Mott insulator.

5.2 Scaling analysis

The scaling is done on the quantity $\mathrm{d}V/\mathrm{d}I$. The full scaling equation is:

$$\frac{\mathrm{d}V}{\mathrm{d}I}(I, f) - \frac{\mathrm{d}V}{\mathrm{d}I}(I_c^{\pm}, f) = \mathcal{F}^{\pm}\left(\frac{|I - I_c^{\pm}|}{h^{(\delta-1)/\delta}}\right) \tag{25}$$

Where $h = |f - f_c|$. The scaling for $f > f_c$ corresponds to $\mathcal{F}^+$ and I_c^+, and for $f < f_c$ corresponds to $\mathcal{F}^-$ and I_c^-, but δ is the same in the whole region. So, if one plots the left hand side on the y-axis and the quantity $|I - I_c^{\pm}|/h^{(\delta-1)/\delta}$ on the x-axis for (f, I) points near (f_c, I_c), these points should collapse onto the curve $\mathcal{F}^{\pm}$.

Figure 14A,B show the unscaled dV/dI traces. The Mott state corresponds to current traces having a local minimum as a function of f, while the metallic state corresponds to current traces having a local maximum as a function of f. $I_c^{\pm}$ is the trace separating these phases (called the separatrix), and it is taken with the criteria $d(dV/dI)/df|_{f=f_c} = 0$. Or in words, starting from a metallic current trace, if one lowers the current, the local minimum will shift to f_c. The current at which this local minimum sits exactly at f_c is I_c (one has to do this procedure both on the $f > f_c$ side and the $f < f_c$ to obtain I_c^+ and I_c^-). The critical current values for (**A**) is $I_c^- = 0.49m$A and $I_0^+ = 0.50m$A and for (**B**) $I_c^- = 0.20m$A and $I_c^+ = 0.23m$A

Figure 14C,D show the scaling. The top panels are plotted semi logarithmically, the bottom panels have the same quantities on the axis, but only the current points larger than

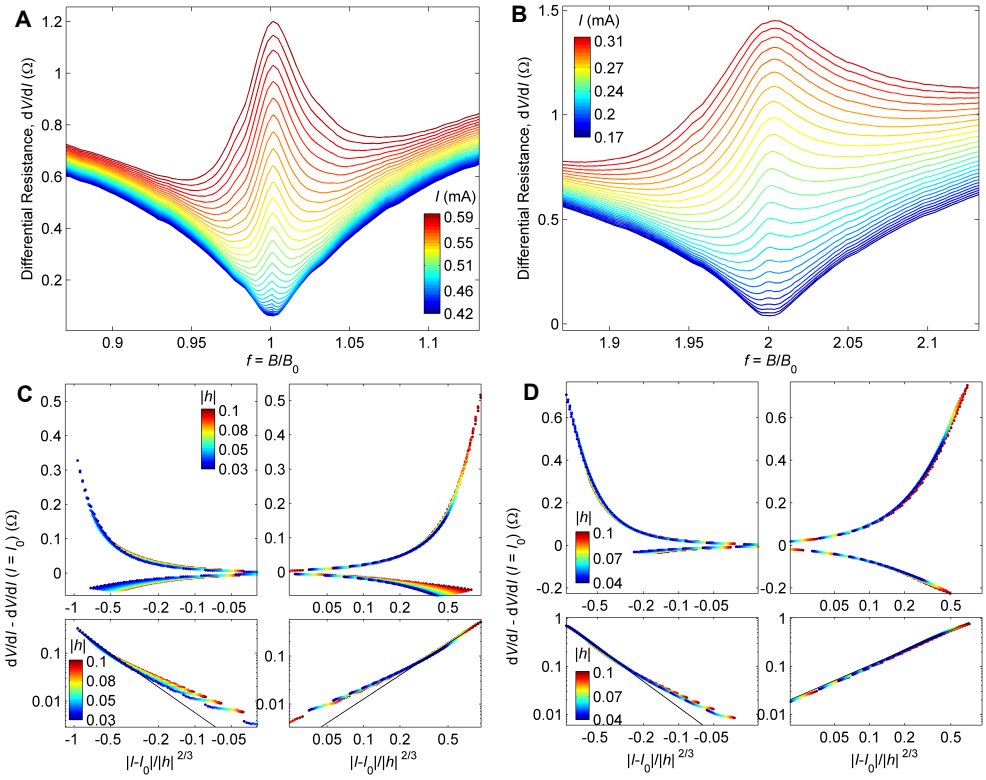

Figure 14: **scaling at integer frustration factors** (**A B**) Separatrix showing the differential resistance as a function of current and magnetic field around the dynamic vortex Mott insulator to metal transition at $f = 1$ and $f = 2$. The separatrix separates the Mott insulator (below) from the metallic state (above). The values for $I_c^{\pm}$ are chosen by the criteria $d(dV/dI)df|_{f=f_c} = 0$ at $I = I_c$. For (**A**) $I_c^- = 0.49mA$ and $I_c^+ = 0.50mA$ and for (**B**) $I_c^- = 0.20mA$ and $I_c^+ = 0.23mA$. (**C D**) Scaling plot with on the y-axis $dV/dI(I, f) - dV/dI(I_c, f)$ and on the x-axis the scaled parameter $|I - I_c|/|h|^{(\delta-1)/\delta}$ with $h = f - f_c$, and I is taken in mA. For both fractions $\delta = 3$. For the upper panels only the x-scale is logarithmic, for the lower panels both the x and y-scales are plotted logarithmic. The linear region is fitted such that $y \propto x^{\mu}$, for (**C**) $\mu = 1.7$ and for (**D**) $\mu = 1.4$.

I_c are shown and both axes are plotted logarithmically. To go from for example 14A to 14C, One first has to define a window of the points in (I, f) space to apply the scaling to. The range for the current points is always taken to range from lowest to the highest shown current trace in the graph. The field range is taken to be $0.03 < h < 0.1$ for 14A, but this range is different for each scaling. For the all the points inside this range, an x value is calculated with $|I - I_c^{\pm}|/h^{(\delta-1)/\delta}$ and the y value is $\frac{\mathrm{dV}}{\mathrm{dI}}(I, f) - \frac{\mathrm{dV}}{\mathrm{dI}}(I_c^{\pm}, f)$. If one plots this one gets figure 14C. For the scaling to work, all points must collapse onto a single curve. The

range is taken to be as big as possible such that this occurs, so points outside of the chosen range do not map onto $\mathcal{F}$. Higher h values do not work because scaling only works near the critical point, and influences of other critical points starts to kick in. Too low values of h do not work, because (I, f) values near the critical point can only scale if the current traces would diverge at f_c, which they do not. For both $f_c = 1$ and $f_c = 2$ is found that $\delta = 3$ scales well. The originally proposed power law behaviour of $\mathcal{F}(x) \propto x^{\mu}$[1] does not hold in the region for small x, so it is possible that this curve should in fact be an exponential function. The difference can be explained by the fact that the x-axis has a larger range. The range extends closer to the origin, and it is only in this range that the power law fit starts to deviate. Finally, the scaling for current values $I > I_c$ the scaling seems to work much better then for $I < I_c$.

In figure 15 the same scaling procedure is done at critical frustration factors with denominator 2, $f_c = 1/2$ and $f_c = 3/2$. Here it is found that for (**A**) $I_c^- = 0.24m\text{A}$ and $I_c^+ = 0.24m\text{A}$ and for (**B**) $I_c^- = 0.116m\text{A}$ and $I_c^+ = 0.122m\text{A}$, and $\delta = 2$. As figure 12 already suggests, the scaling is different than for integer critical frustration factors. This is attributed to the different statistics of the vortex sea. For integer filling, the statistics can be seen as ferromagnetic, because the magnetic moments corresponding to the vortices are all aligned, and is associated with the Ising universality class. In the half integer case the corresponding statistics are anti-ferromagnetic because magnetic moments corresponding to the vortices are aligned anti-ferromagnetically, and thus the universality class is different.

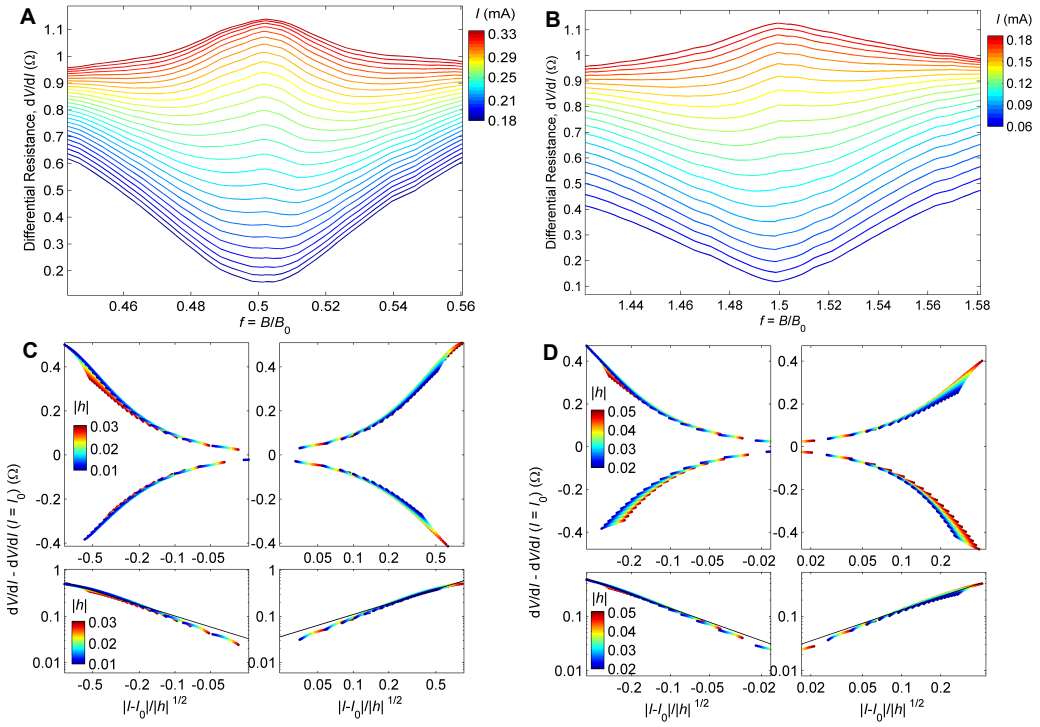

Figure 15: **scaling at frustration factors with denominator** 2 (**A B**) Separatrix showing the differential resistance as a function of current and magnetic field around the dynamic vortex Mott insulator to metal transition at $f = 1/2$ and $f = 3/2$. The separatrix separates the Mott insulator (below) from the metallic state (above). The values for $I_c^{\pm}$ are chosen by the criteria $d(dV/dI)df|_{f=f_c} = 0$ at $I = I_c$. For (**A**) $I_c^- = 0.24m$A and $I_c^+ = 0.24m$A and for (**B**) $I_c^- = 0.116m$A and $I_c^+ = 0.122m$A. (**C D**) Scaling plot with on the y-axis $dV/dI(I, f) - dV/dI(I_c, f)$ and on the x-axis the scaled parameter $|I - I_c|/|h|^{(\delta-1)/\delta}$ with $h = f - f_c$, and I is taken in mA. For both fractions $\delta = 2$. For the upper panels only the x-scale is logarithmic, for the lower panels both the x and y-scales are plotted logarithmic. The linear region is fitted such that $y \propto x^{\mu}$, for (**C**) $\mu = 0.78$ and for (**D**) $\mu = 0.83$.

6 Temperature dependence and Thermal activation

At a finite temperature several elementary types of excitations exist: phase slips, formation of vortices (or vortex-anti vortex pairs) and the jump of a vortex to a neighbouring site. All these processes require overcoming a energy barrier, so these processes can be thermally activated as the thermal energy k_BT approaches the height of the barrier. Contrary, for arrays where damping is small, i.e. $E_J >> E_C$, quantum effect play a role and it is possible for the state to tunnel through the potential barrier. In this case, at low temperatures the thermal activation freezes out, but there is still a finite probability (with an associated tunnel attempt frequency) for tunnelling to occur through the barrier. Considering the observation that the $I(V)$ curves of the fabricated arrays show damped behaviour (so C is small, so $E_C \propto 1/C$ is large), one would expect thermally activated behaviour. This section is devoted to proving experimentally that this thermal activation occurs in our device and obtain its dependence on the external current. To this extent the resistance is measured as a function of current and temperature (at a fixed magnetic field of $f = 1$ and $f = 1/2$). This data can be used to obtain an Arrhenius type of energy barrier with the relation $R \propto \exp -E_b/k_BT$. In the second section the implications will be discussed. For comparison, [30] shows temperature dependent measurements that were done on samples of larger dimensions.

6.1 Experiments

In figures 16 and 17 the temperature evolution of both the resistance and differential resistance is shown as a function of external current at $f = 1$ and $f = 1/2$ respectively. In figure 22 in appendix C measurements with a varying field are also shown. The top left panel shows the resistance and the top right panel shows the differential resistance. The bottom left panel shows an Arrhenius plot. For both field values, it is clear that the relation $R \propto \exp -E_b/k_BT$ holds below the critical temperature. An offset resistance was subtracted of $19.4m\Omega$ for figure 16 and $17.3m\Omega$ for figure 17 in the Arrhenius plot. This resistance is attributed to the gap between the Nb bars and the onset of the islands. Note that these values are approximately the same as the value found in the Ambegaokar Halperin fit in section 4.2. The value of this offset can be read off quite accurately simply by taking the lowest resistance of any current and temperature, but the Arrhenius plot is also very sensitive to any error in this value. Therefore a range of reasonably possible offset resistances were tried and it is concluded that in the whole range the curves remain linear below T_c. In the bottom right panel the obtained energy barrier as a function of current is shown, and it is fitted with the relation $\Delta U(I) = 2E_J(1 - I/I_{c0})^{3/2}$ which is the barrier height for a single Josephson Junction. This is the energy barrier which the system has to overcome for the phase to slip, which is one of the candidates for the excitation mechanism, see section 6.2. This relation fits the data qualitatively for the $f = 1$ case, but for the $f = 1/2$ case the barrier height is obtained in a larger current range (scaled to I_{c0}), causing the fit not to work in this case. Counter-intuitively, the barrier energy for $f = 1/2$ seems larger than for $f = 1$.

The experiments show that the process is thermally activated in the range $I < I_c(T)$ as one would expect. However, this does not answer which mechanism occurs. One could investigate this energy barrier as a function of current and the whole field range $E_B(f, I)$ and compare this with theoretical models, or experimentally, use scanning SQUID measurements to directly probe the evolution of the vortices in space and time.

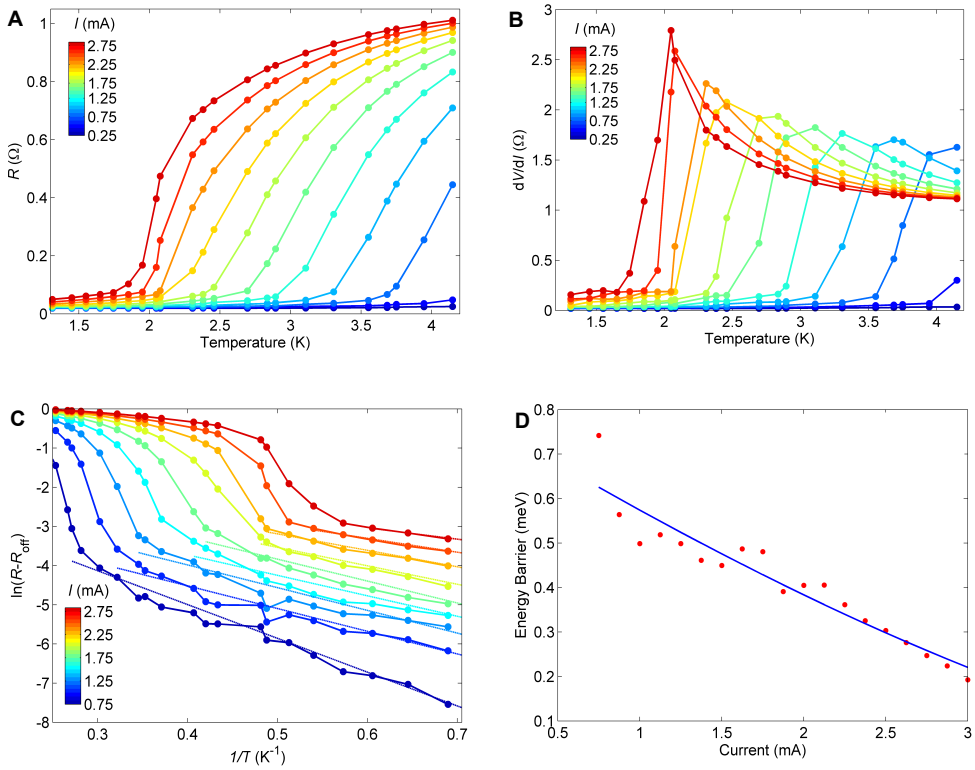

Figure 16: **Temperature dependence and Thermal activation at $f = 1$** (**A B**) Resistance and Differential resistance as a function of temperature at $f = 1$ at various current values. (**C**) Arrhenius plot of the resistance curves. Below a certain temperature such that $k_B T$ is much smaller than the energy barrier, the data is thermally activated so $R \propto \exp -E_b/k_B T$ where E_b is the energy barrier. The $R(T)$ curve should be linear in an Arrhenius plot at sufficiently low temperatures. (**D**) The values for the energy barrier obtained from the Arrhenius fits are plotted as a function of current, corresponding to the red dots. To give an indication, the blue line is a fit $\Delta U(I) = 2E_J(1 - I/I_{c0})^{3/2}$ which is the barrier height for a single Josephson Junction.

6.2 Activation mechanism

The aim of this section is to give some qualitative insight in how the barrier should depend on external current for the different processes.

1. Phase slips: The dependence of phase slips on external current is caused by the tilting of the potential. As the current is increased, the potential landscape is tilted and the barrier height decreases. The fit in figure 16 is the relation between current and energy barrier for a single Josephson Junction, as it is expected to be qualitatively the same

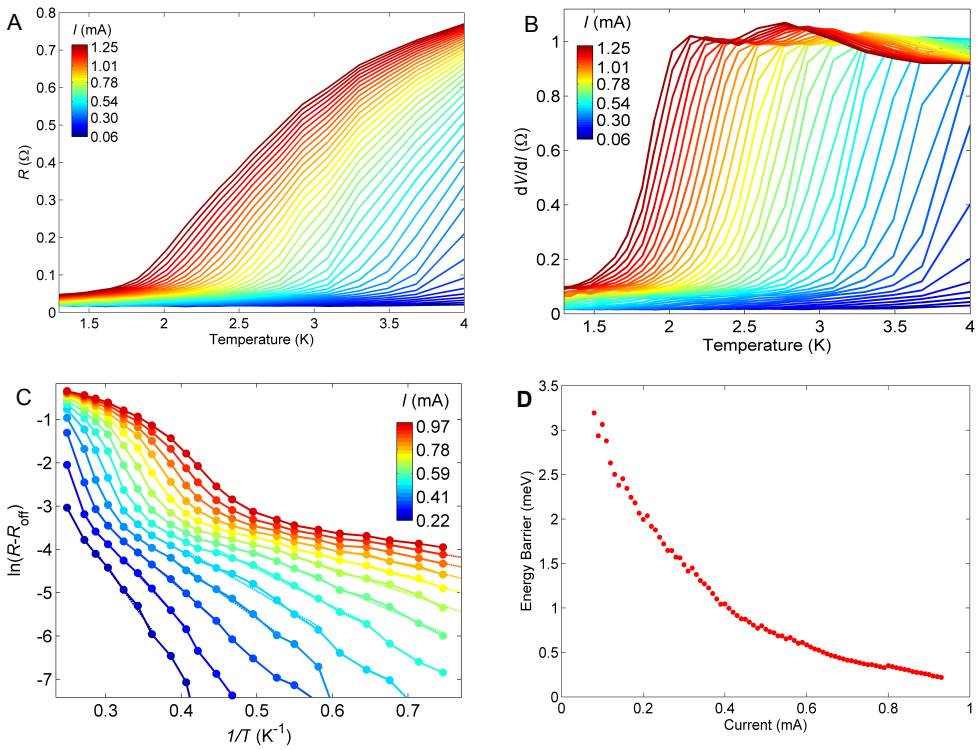

Figure 17: **Temperature dependence and Thermal activation at** $f = 1/2$ Same graph as figure 16 but now for $f = 1/2$. The Arrhenius fit in panel **C** is done in a bigger current range than for $f = 1$. In panel **D** no fit is shown because the fit used for $f = 1$ does not follow the curve.

for an array. In principle one must also take into account the attempt frequency, which is also a function of current, but this is neglected.

2. formation of vortices: The energy needed to create or destroy a vortex depends very much on the vortex configuration surrounding the vortex. In section 3.5 the formation of vortices and vortex-antivortex pairs in the zero-field ground state is discussed. When one applies an external magnetic field, complex vortex patterns will emerge complicating this picture. Also the creation of vortices depends on the value $< n > -f$, where $< n >$ is the mean number of vortices, because any deviation from this induces an energy which is proportional to the size of the array, and in fact in the measured arrays this quantity is always approximately zero. So, if a vortex is created, quickly a vortex must also be annihilated, or the vortices must come in vortex-antivortex pairs. In zero magnetic field it is known that below some temperature called the Kosterlitz-Thouless temperature, vortex-antivortex pairs are created rather than single vortex excitations

because it is energetically more favourable. However upon increasing the temperature, at T_{KT} a phase transition occurs where now single vortex excitations become feasible. However in this range, the free vortices cause a linear resistance. When a current is applied below T_{KT}, the current breaks up the vortex-antivortex pairs, due to the opposite Lorentz force [31].

3. moving of vortices: The movement of vortices is induced by an external current via the Lorentz force, analogous to the depinning in bulk superconductors. This has qualitatively the same effect that the energy barrier for moving vortices is decreased as current is increased.

From these considerations the measurements do not illuminate the precise microscopic behaviour of the vortices and more investigation is needed.

7 Conclusion and Recommendations

7.1 Conclusion

We have fabricated square Josephson Junction Arrays of 300 by 300 niobium islands on a sheet of gold. On this sample, the voltage is measured as a function of current and magnetic field at $4.2K$ in a bath cryostat. From this data the critical current as a function of magnetic field is obtained, which show peaks at rational values of $f = B/B_p$, where B_p is found to be equal to the Φ_0 divided by the area of an elementary plaque. This is attributed to the formation of a periodic vortex lattice. Most fractions with a denominator of 6 or lower can be observed.

Furthermore, at $f = 1$ and $f = 1/2$ the resistance is measured as a function of current and temperature from 4.2K to 1.3K. Below the critical temperature the Arrhenius relation holds, proving that the vortices are thermally activated, and in this temperature range do not undergo quantum tunnelling. From this Arrhenius fit an energy barrier can be obtained as a function of current. This is fitted with the energy barrier relation for a single Josephson Junction, which qualitatively agrees with the data at $f = 1$, but does not work for $f = 1/2$.

Around rational values of f, the differential resistance as a function of f is found to have a minimum at $f = f_c$ which turns into a maximum as the current is increased past the critical current. This phase transition is found to scale as $|I - I_c| \propto |f - f_c|^{2/3}$ for integer frustrations $f_c = 1$ and $f_c = 2$, and as $|I - I_c| \propto |f - f_c|^{1/2}$ for frustrations with denominator 2 $f_c = 1/2$ and $f_c = 3/2$. This phase transition is attributed to statistics of the sea of vortices, forming a Mott vortex insulator to metal transitions. This transition is analogous to an electronic Mott insulator to metal transition where the vortices here play the role of electrons in the electronic Mott insulator to metal transition. This opens the possibility to use vortices in JJAs as a laboratory system to study strongly correlated systems.

Finally it is shown that the tilted washboard potential for a single Josephson Junction can be generalized to arbitrary Josephson Junction Arrays. A computer model was made which numerically finds the equilibrium states energies and current configurations as a function of external current and external magnetic field. Only proof of concept computer experiments were done on this, showing an incomplete energy spectrum on a square JJA with 10 by 10 islands. In principle the full energy spectrum of finite Josephson Junction arrays can be studied, and also the effect of disorder.

7.2 Recommendations

For further research, the scaling transition can be measured as a function of temperature, to see if δ is independent of temperature. Also scaling at other fractions can be done, which could lead to the discovery of new universality classes. Also measuring at temperatures in the mK range can illuminate in more detail the complex underlying potential landscape, perhaps allowing the scaling analysis at more fractions. Furthermore, hysteretic effects and quantum effects might come into play as thermal activation is frozen out.

Measuring the sea of vortices with scanning SQUID spectroscopy can provide valuable information about the structure of the vortices. It can provide an evolution of the ground state vortex configuration as a function of magnetic field, and even give some insight in the actual mechanism of the dynamics of the vortices in the voltage state. The tilted washboard

potential can be used to calculate the ground state vortex configuration as a function of magnetic field, and this can be compared to the Scanning SQUID measurements.

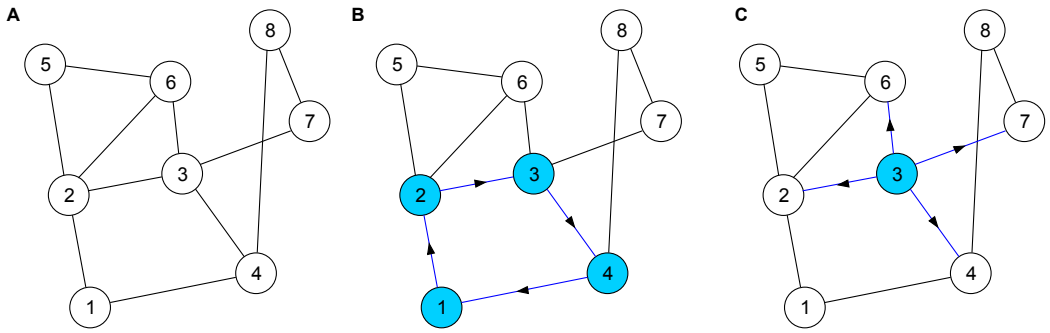

Figure 18: **Graph theory concepts** (**A**) Example of a graph g with vertices $\{1,2,3,4,5,6,7,8\}$ and edges $\{(1\,2),(1\,4),(2\,3),(2\,5),(2\,6),(3\,4),(3\,6),(3\,7),(4\,8),(5\,6),(7\,8)\}$. (**B**) An example of a cycle in g with as vertices $\{1,2,3,4\}$, as edges $\{(1\,2),(1\,4),(2\,3),(3\,4)\}$ and as subgraph vector $(1,-1,1,0,0,1,0,0,0,0,0)$. (**C**) An example of a neighbourhood in g with as vertex 3, as edges $\{(2\,3),(3\,4),(3\,6),(3\,7)\}$ and as subgraph vector $(0,0,-1,0,0,1,1,1,0,0,0)$.

A Derivation of potential formulation JJAs

This section will contain a mathematical derivation of the tilted washboard model for arrays. To be able to state the theorem, graph theory will be used. Starting from a undirected connected simple graph, first some definitions are needed:

Definition A.1. Cycle: a cycle in g is a directed subgraph of the undirected graph g. The edges and vertices are those corresponding to any closed simple walk in g, and the direction of the edges is in the direction of the walk.

Definition A.2. Neighbourhood: a neighbourhood in graph g of vertex $v \in V$ is a directed subgraph of the undirected graph g. It contains the vertex v and all edges connected to v. The direction of the edges are pointing away v.

Definition A.3. Subgraph vector: a subgraph vector is a vector $\vec{a}$ corresponding to a graph g ans subgraph $g' \subset g$ with the same amount of components as there are edges in graph g. The value of a component is 0 if that edge is not present in g', 1 if that edge is present in g' and the edge points to the higher vertex of the edge, and -1 if it points to the lower vertex of the edge.

As a convention, all the vertices in g are numbered, and the edges are denoted by the vertex numbers it connects, so edge(12) connects vertices 1 and 2. Edges are always denoted in ascending order. In figures 18 these definitions are illustrated.

The goal will be to prove the following:

Given any undirected connected simple graph g with edges E and vertices V. One imposes on this two kinds of directed subgraphs, called cycles and neighbourhoods. The set of all cycles p is called P, the set of all neighbourhoods n is called N. Take A to be a matrix whose rows are all subgraph vectors in P and M to be a matrix whose rows are all subgraph

vectors in N. Then to each edge e one assigns two numbers, $b_e \in \mathbb{R}$ and $\theta_e \in [-\pi, \pi)$, and put them in the vectors $\vec{b}$ and $\vec{\theta}$. To each neighbourhood n one assigns a number $I_n \in \mathbb{R}$ and puts it in the vector $\vec{I}_{\text{ext}}$. Than the goal is to to prove that the system in which $\vec{\theta}$ is the only unknown:

$$\begin{aligned} A\vec{\theta} &= \vec{b} \\ MI_c \sin\vec{\theta} &= \vec{I}_{ext} \end{aligned}$$

Has the same solution for $\vec{\theta}$ as the following system:

$$\begin{aligned} \text{find stationairy point of: } u &= \sum_{(ij)\in E} (I_c(1-\cos\theta_{ij}) - c_{ij}\theta_{ij}I) \\ \text{subject to: } A\vec{\theta} &= \vec{b} \\ M\vec{c}I &= \vec{I}_{ext} \end{aligned}$$

Where $u = U/\Phi_0$. The proof is done in two steps. First Lagrange multipliers are used on the potential u to obtain a system of equations. Then in step two the equivalence of this system to the first system is shown. So first one sets up the Lagrangian:

$$\Lambda = u + (A\vec{\theta} - \vec{b}) \cdot \vec{\lambda} \tag{26}$$

And the new equations are:

$$\frac{\mathrm{d}\Lambda}{\mathrm{d}\theta_{ij}} = 0; \tag{27}$$

$$I_c \sin\vec{\theta} - \vec{c}I + A^T\vec{\lambda} = 0; \tag{28}$$

Now one can eliminate the λ's with the following trick:

$$\text{for any matrix } A\text{: } A \cdot \text{Null}(A) = 0 \tag{29}$$

$$\text{Null}(A)^T \cdot A^T = 0 \tag{30}$$

$$\text{Null}(A)^T \cdot A^T \cdot \vec{\lambda} = 0 \tag{31}$$

$$\text{Null}(A)^T \cdot -(I_c \sin\vec{\theta} - \vec{c}I) = 0 \tag{32}$$

or

$$\text{Null}(A)^T \cdot (I_c \sin\vec{\theta} - \vec{c}I) = 0 \tag{33}$$

This combined with $A\vec{\theta} = \vec{b}$ now looks like system one. If one could prove that the rowspaces of M and $\text{Null}(A)^T$ are the same vector space, then the equation reduces to the

second equation of system one if and only if $M\vec{c}I = \vec{I}_{\text{ext}}$. The rest of this section is devoted to proving this statement.

This is a general graph theoretical problem. The rowspace A is called the Cycle space and the rowspace of M is exactly the edge cut space. It is known that these two spaces are orthogonal. This proves the theorem. [32]

Note, the rank of the cycle space of a connected graph is $n-m+1$, where n is the number of edges and m is the number of vertices. So this is the maximal number of cycles one needs to form a spanning basis of the space. One can use the greedy algorithm to compute a basis for the cycle space. The rank of the edge cut space is $m-1$, corresponding to the m Kirchhoff's rules minus one because the sum of all Kirchhoff's rules is zero. The sum of these is exactly the number of edges, which means that system one has precisely the same number of equations as unknowns.

B Circuit diagram

In figure B the circuit diagram is shown which describes the experimental setup for the IV measurements. A homebuilt current-source is used to source a triangle wave of approximately 1Hz. Typically for one $V(I)$ curve 20k samples were taken at a sampling rate of 5k. The resulting data is then binned to very small equal sized current bins. Then the Matlab smoothing method loess is used to smooth the $V(I)$ curves.

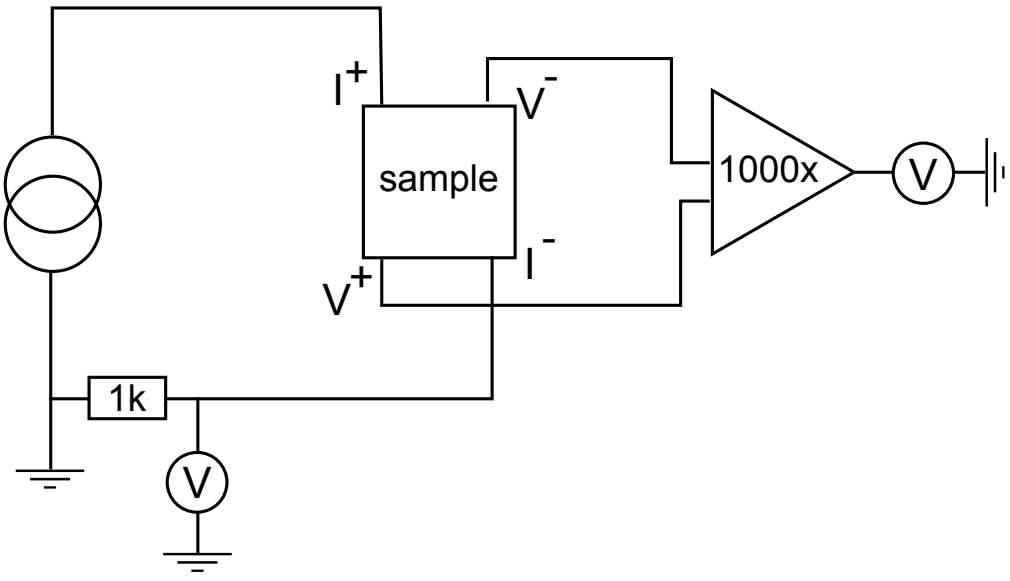

Figure 19: Electrical circuit used to measure the $I(V)$ curves on the JJA. The bottom voltmeter is used to measure the current and the right voltmeter is used to measure the voltage.

C Temperature dependant measurements

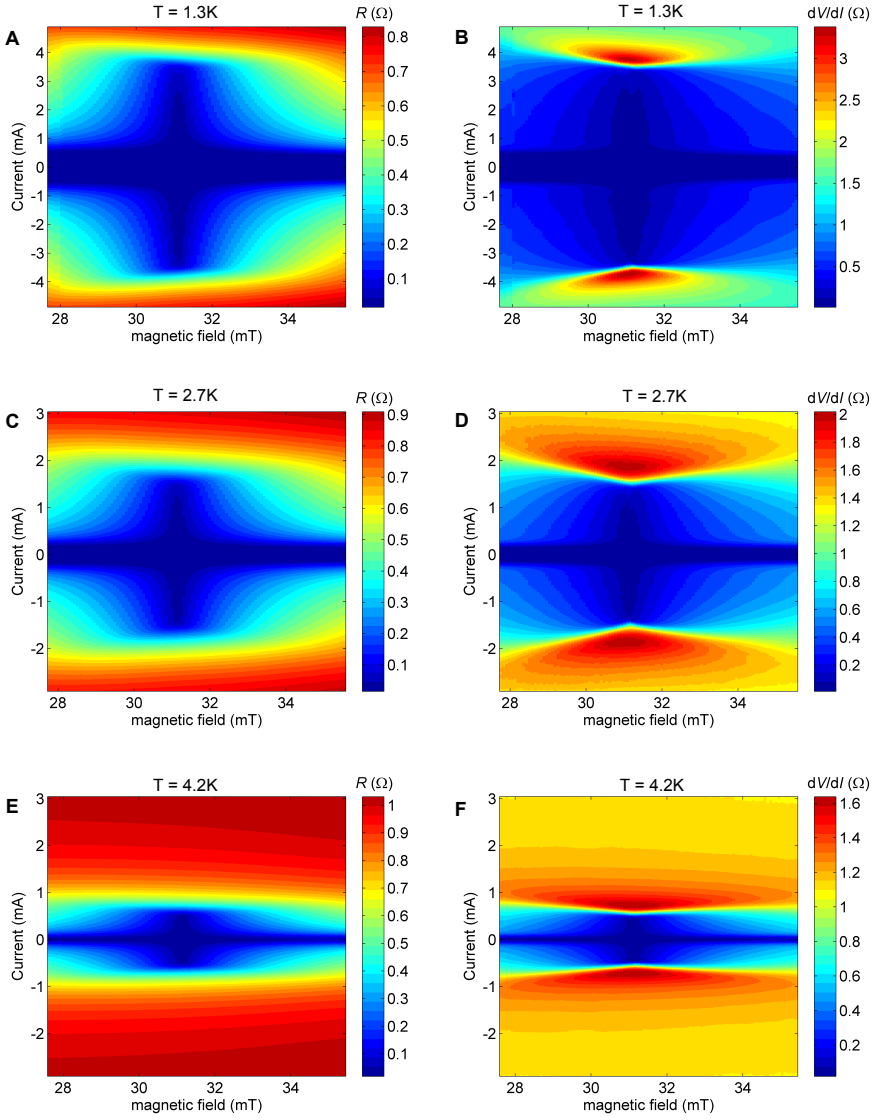

Figure 20: **resistance and differential resistance as a function of temperature and field** (**A C E**) resistance and (**B D F**) differential resistance at three different temperatures around the value $f = 1$. It can be seen that the resistance as a function of temperature approximately only stretches in I, so $R(I, B, T) = \hat{R}(f(I, T), B)$.

D Ground state current configurations

In this section the ground state current configuration of $f = 1/3$ and $f = 1/2$ as calculated with the tilted washboard model for arrays on square array with 10 by 10 islands are shown.

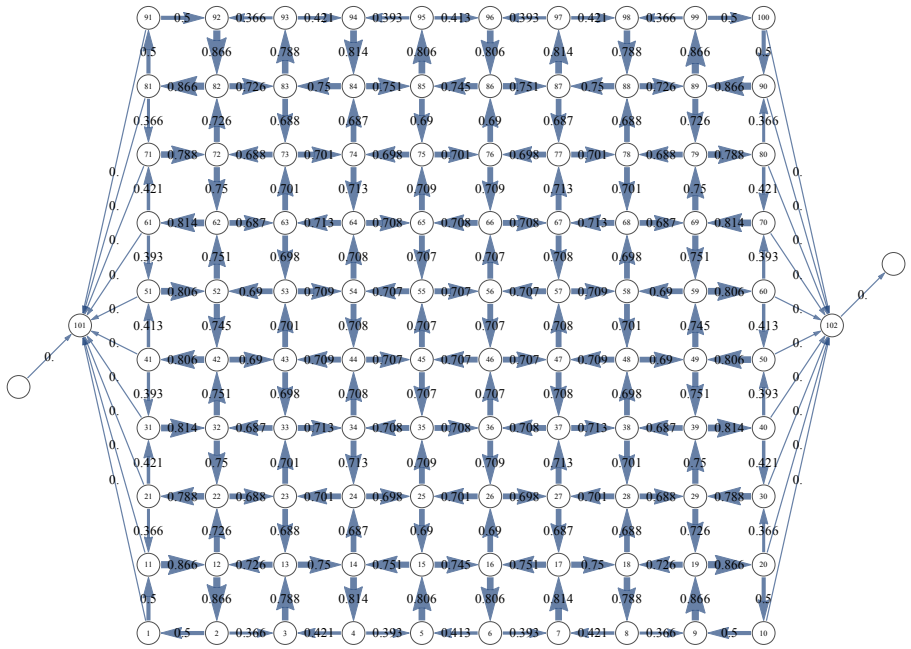

Figure 21: Current distribution in an array with as vortex configuration the ground state vortex configuration at $f = 1/2$, as field $f = 1/2$ and no external current.

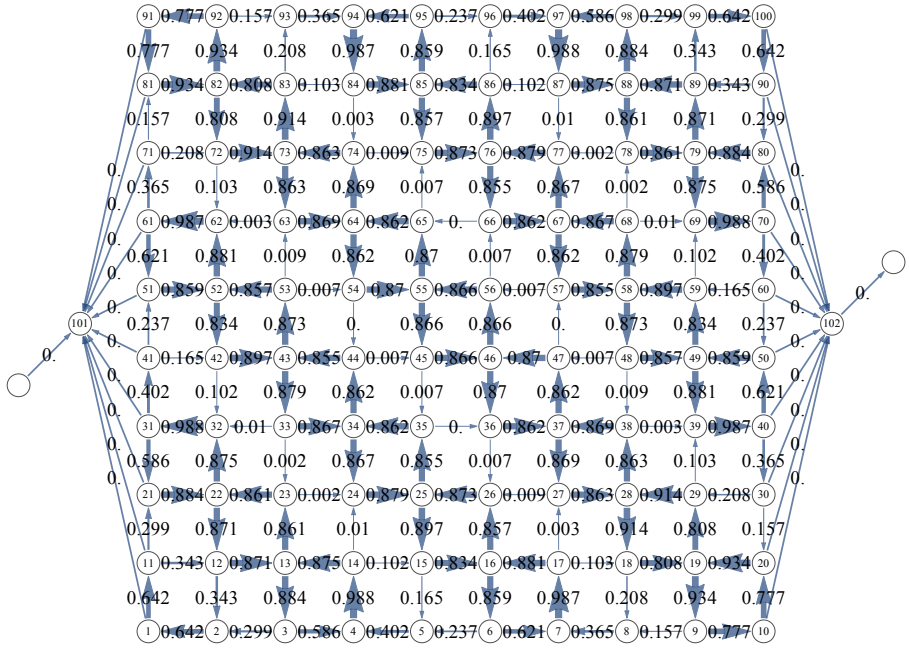

Figure 22: Current distribution in an array with as vortex configuration the ground state vortex configuration at $f = 1/3$, as field $f = 1/3$ and no external current.

References

[1] N.Poccia, T.I.Baturina, F.Coneri, C.G.Molenaar, X.R.Wang, G.Bianconi, A.Brinkman, H.Hilgenkamp, A.A.Golubov, V.M.Vinokur. Critical behavior at the dynamic mott transition. *arXiv*, page 1408.5525, 2014.

[2] J.Zaanen. High-temperature superconductivity: The benefit of fractal dirt. *Nature*, 466:825–826, 2010.

[3] P. Littlewood. Superconductivity: An x-ray oxygen regulator. *Nature mat.*, 10:726–727, 2011.

[4] E. Dagotto. Colloquium: The unexpected properties of alkali metal iron selenide superconductors. *Rev. Mod. Phys.*, 85:849–867, 2013.

[5] A. Bianconi. Quantum materials: Shape resonances in superstripes. *Nat. Phys.*, 9:536–537, 2013.

[6] M.Fratini, N.Poccia, A.Ricci, G.Campi, M.Burghammer, G.Aeppli, A.Bianconi et al. Scale-free structural organization of oxygen interstitials in La_2CuO_{4+y}. *Nature*, 466:841–844, 2010.

[7] N.Poccia, A.Ricci, G.Campi, M.Fratini, A.Puri, D. Di Gioacchino, A.Marcelli, M.Reynolds, M.Burghammer, N.L.Saini, et al. Optimum inhomogeneity of local lattice distortions in La_2CuO_4. *National Acad. Sciences*, 109(39):15685–15690, 2012.

[8] A.Ricci, N.Poccia, G.Campi, B.Joseph, G.Arrighetti, L.Barba, M.Reynolds, M.Burghammer, H.Takeya, Y.Mizuguchi, et al. Nanoscale phase separation in the iron chalcogenide superconductor $K_{0.8}Fe_{1.6}Se_2$ as seen via scanning nanofocused x-ray diffraction. *Phys. Rev. B*, 84(6):060511, 2011.

[9] N.Poccia, M.Fratini, A.Ricci, G.Campi, L.Barba, A.Vittorini-Orgeas, G.Bianconi, G.Aeppli, A.Bianconi. Evolution and control of oxygen order in a cuprate superconductor. *Nature Mat.*, 10(10):733–736, 2011.

[10] B.Phillabaum, E.W.Carlson, and K.A.Dahmen. Spatial complexity due to bulk electronic nematicity in a superconducting underdoped cuprate. *Nature Communications*, 3:915, 2012.

[11] N.Poccia, A.Ricci, A.Bianconi. Fractal structure favoring superconductivity at high temperatures in a stack of membranes near a strain quantum critical point. *Journal of Superconductivity and Novel Magnetism*, 24(3):1195–1200, 2011.

[12] G.Bianconi. Superconductor-insulator transition on annealed complex networks. *Phys. Rev. E*, 85(6):061113, 2012.

[13] G.Bianconi. Superconductor-insulator transition in a network of 2d percolation clusters. *EPL*, 101(2):26003, 2013.

[14] I.Bloch, W.Zwerger. Many-body physics with ultracold gases. *Reviews of Modern Physics*, 80:855–961, 2008.

[15] M.Greiner, O.Mandel, T.Esslinger, T.W.Hänsch, I.Bloch. Quantum Phase Transition from a Superfluid to a Mott Insulator in a Gas of Ultracold Atoms. *Nature*, 415:39–44, 2002.

[16] D.Fisher. Sliding charge-density waves as a dynamic critical phenomenon. *Phys. Rev. B*, 31(3):1396–1427, 1985.

[17] D.Nelson, V.Vinokur. Boson localization and correlated pinning of superconducting vortex arrays. *Phys. Rev. B*, 48(17):13060–13097, 1993.

[18] D.Nelson, V.Vinokur. Boson localization and pinning by correlated disorder in high-temperature superconductors. *Phys. Rev. Lett*, 68(15):2398–2401, 1992.

[19] M.Tinkham. *Introduction to Superconductivity*. Dover, 2 edition, 1996.

[20] V.Ambegaokar, B.I.Halperin. Voltage due to thermal noise in the DC Josephson effect. *Phys. Rev. Lett.*, 22(25):1364–1366, 1969.

[21] H.Fazio, H.v.d.Zant. Quantum phase transitions and vortex dynamics in superconducting networks. *Phys. Rep.*, 355(4):235–334, 2001.

[22] D.R.Hofstadter. Energy levels and wave functions of bloch electrons in rational and irrational magnetic fields. *Phys. Rev. B*, 14(6):2239–2249, 1976.

[23] B.Pannetier, J.Chaussy, R.Rammal, and J.C.Villegier. Experimental Fine Tuning of Frustration: Two-Dimensional Superconducting Network in a Magnetic Field. *Phys. Rev. Lett*, 53(19):1845–1848, 1984.

[24] R.Théron, S.E.Korshunov, J.B.Simond, Ch.Leemann, P.Martinoli. Observation of domain-wall superlattice states in a frustrated triangular array of josephson junctions. *Phys. Rev. Lett.*, 72(4):562–565, 1994.

[25] S.Eley,S.Gopalakrishnan, P.M.Goldbart, N.Mason. Approaching zero-temperature metallic states in mesoscopic superconductor–normal–superconductor arrays. *Nat. Phys.*, 8:59–62, 2012.

[26] K.H.J. Buschow. *Concise Encyclopedia of Magnetic and Superconducting Materials*. Elsevier, 2 edition, 2005.

[27] Z.Jiang, D.A.Dikin, V.Chandrasekhar, V.V.Metlushko, V.V.Moshchalkov. Pinning phenomena in a superconducting film with a square lattice of artificial pinning centers. *Appl. Phys. Lett*, 84(26):5371–5373, 2004.

[28] G.Kotliar, E.Lange, M.J.Rozenberg. Landau Theory of the Finite Temperature Mott Transition. *Phys. Rev. Lett.*, 84(22):59–62, 2000.

[29] P.Limelette, A.Georges, D.Jerome, P.Wzietek, P.Metcalf, J.M.Honig. Universality and critical behavior at the mott transition. *Science*, 302(5642):89–92, 2003.

[30] R.A.Webb, R.F.Voss, G.Grinstein, P.M.Horn. Magnetic Field Behavior of a Josephson-Junction Array: Two-Dimensional Flux Transport on a Periodic Substrate. *Phys. Rev. Lett.*, 51(8):690–693, 1983.

[31] D.J.Resnick, J.C.Garland, J.T.Boyd, S.Shoemaker an R.S.Newrock. Kosterlitz Thouless Transition in proximity-coupled superconducting arrays. *Phys. Rev. Lett.*, 47(21):1542–1545, 1981.

[32] J.L.Gross, J.Yellen. *Graph Theory and Its Applications.* Chapman and Hall/CRC, 2 edition, 2005. section 4.6.